

Finite element modeling of extraordinary optoconductance in GaAs-In metal-semiconductor hybrid structures

K. A. Wieland, Yun Wang, and S. A. Solin*

*Department of Physics and Center for Materials Innovation,
Washington University in St. Louis, CB 1105, 1 Brookings Drive, St. Louis, MO 63130*

A. M. Girgis and L. R. Ram-Mohan

Department of Physics, Worcester Polytechnic Institute, Worcester, MA 01609

(Dated: Converted to LaTeX February 8, 2020)

We present a detailed discussion of extraordinary optoconductance (EOC). Experimental data was acquired via macroscopic metal-semiconductor hybrid structures composed of GaAs and In and subjected to illumination from an Ar ion laser. A drift diffusion model using the finite element method (FEM) provided a reasonable fit to the data. EOC is explored as a function of laser position, bias current, laser power density, and temperature. The positional dependence of the voltage is accounted for by the Dember effect, with the model incorporating the excess hole distribution based on the carrier mobility, and thus the mean free path. The bias current is found to produce a linear voltage offset and does not influence the EOC. A linear relationship is found between the laser power density and the voltage in the bare and hybrid devices. This dependence is reproduced in the model by a generation rate parameter which is related to the power density. Incorporating the mobility and diffusion temperature dependence, the model directly parallels the temperature dependence of the EOC without the use of fitting parameters.

PACS numbers: 72.20.Jv, 72.40.+W, 72.80.Ey

I. INTRODUCTION

The resistance of any device can be divided into two components, one physical and one geometric. Contributions to the physical component arise from factors such as the doping levels, impurities, bulk conductivity, and bulk mobility. The geometric contributions arise from factors such as the device dimensions, shape, and arrangement of the leads as well as any inhomogeneities that may be present. Most often, the physical contributions dominate the resistance, but by judicious choices, the geometric component can become the dominant component. The recently discovered EXX effects¹ in metal-semiconductor hybrid structures (MSHs) of the type shown schematically in Fig. 1(b) are primarily geometric in nature and rely on a reallocation of current between the metal and semiconductor regions due to an external perturbation. Here XX refers to magnetoresistance (MR), piezoconductance (PC), etc. The perturbation can alter the interface between the metal and semiconductor regions or, as we show here, the bulk transport characteristics of either constituent. If the metal and semiconductor conductivities differ by several orders of magnitude, as is the case with GaAs and In, small perturbations can dramatically change the flow of current through the device. As a result, under perturbation, the measured voltage difference (depicted as V_{MSH} in Fig. 1(b)) increases as compared to that of the metal or semiconductor alone. The large, often linear, change in voltage makes EXX devices an excellent choice for high resolution spatial sensing. Additionally, because they are non-magnetic, EXX devices can be used in applications where typical magnetic sensors are not suitable.²

The original EXX effect to be discovered was EMR.³ An InSb-Au MSH structure of macroscopic (and later nanometer) dimensions was fabricated using novel techniques described elsewhere.⁴ The perturbation in this case was a magnetic field, redirecting the current through the semiconductor, whereas that current flows primarily through the metal with no applied field. A room temperature EMR of order 10⁶% was observed at fields of 5T. Theoretical modeling of EMR, using the finite element method (FEM) incorporating the effects of the boundary conditions at the metal-semiconductor interface, has shown excellent agreement with the experimental data.^{5,6} EMR has potential applications in a number of diverse areas including ultra-high-density magnetic recording, position sensing, and medical instrumentation. Scanning EMR probes have also been proposed as a way to concurrently measure topographic and magnetic field information with high spatial and temporal resolution.⁷

The second demonstrated EXX effect was EPC.⁸ An InSb-Au MSH structure, similar to that used for EMR, was constructed. In EPC the perturbation is a uniaxial tensile strain of the metal-semiconductor interface. Room temperature extraordinary piezoconductance as high as 500% has been demonstrated in the above described MSH structures.⁸ Theoretical models based on both the FEM solution and the analytic solutions of Laplace's equation have accurately reproduced the EPC effect.¹ EPC devices have obvious applications in the construction industry and have also been proposed for studying basic material properties (interface dynamics).

Following the discovery of EMR and EPC it was realized that an optical equivalent of the EXX phenomena, e.g. extraordinary optoconductance or EOC, should ex-

ist, with photons providing the perturbation. Such a device would have applicability in the solar energy field, modern fiber optic relays, position sensors, and other optoelectronic devices. We have recently provided a proof of principle demonstration of the EOC effect in GaAs-In MSH structures in a brief preliminary report.⁹ Here we give a full account of this effect and show a detailed FEM calculation that quantitatively accounts for the observed experimental results.

A diagram of an MSH device is given in Fig. 1(b) with the connections shown schematically. The mesh shown in Fig. 1(c) contains fewer elements than the actual mesh used for calculations. The bare device has the same physical connections as shown in Fig. 1(a). In a voltage measurement, the surface of the semiconductor region is exposed to a focused laser beam, whose lateral position (x_ℓ, y_ℓ) can be accurately controlled (see experimental details below). We define EOC as the percent difference in the measured output voltage in the MSH, as compared to that of the bare semiconductor with no shunt attached, such that

$$EOC(x_\ell, y_\ell, \lambda, \{\beta\}) = \left(\frac{[V_{23}(x_\ell, y_\ell)]_{MSH} - [V_{23}(x_\ell, y_\ell)]_{bare}}{[V_{23}(x_\ell, y_\ell)]_{bare}} \right) \times 100\%. \quad (1)$$

Here the parameter set $\{\beta\}$ represents the power density of the laser, P , the temperature, T , and the bias current I . The quantity $\lambda = 476.5$ nm is the emission wavelength of the laser, which is held fixed for all experiments. In this paper, we investigate the EOC as a function of the laser spot position with the parameters $\{\beta\}$ held fixed, and as a function of each of the $\{\beta\}$ parameters with the spot position and the other parameters in the set held fixed. Because of the many factors influencing EOC, it presents a unique opportunity to study the dynamics of the metal semiconductor interface, carrier transport phenomena, and the effect of introducing a shunt.

II. EXPERIMENT

A. Experimental Setup

The experimental setup used to measure the EOC is shown in Figure 2. The bare (shuntless) sample was illuminated with a Coherent Innova 400 Ar+ ion laser operating at 476.5 nm with the beam focused to a 20 μ m diameter. The power density was varied from 6.3×10^4 W/cm² to 5.8×10^6 W/cm². The samples were mounted in an ARS closed cycle helium cryostat and cooled to temperatures ranging from 10 K - 300 K. The cryostat temperature was maintained by a Scientific Instruments 9650 temperature controller. The sample was positioned using a Newport Universal Motion Controller ESP 300 system with three linear DC stepper motors. For optimal spatial resolution, the sample was placed at the focused beam waist, thereby defining the distance from

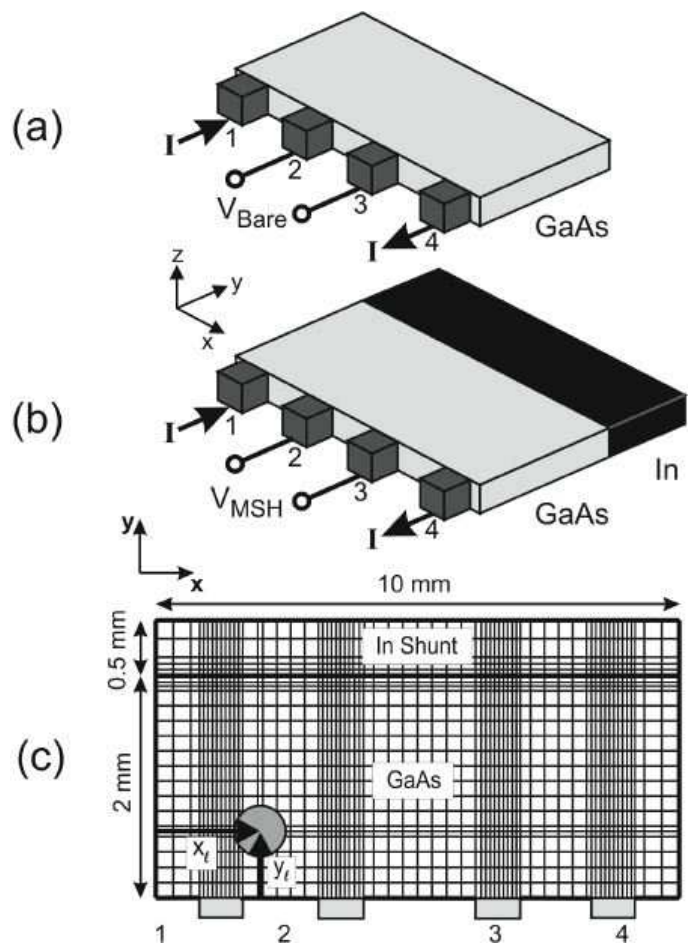


FIG. 1: (Color online) Bare (a) and MSHs (b) devices. (c) The FEM mesh showing the device dimensions, port configuration, and schematic of the connections to the device.

the lens to the sample and the diameter of the laser spot. The bias current was supplied by a Lakeshore 120 current source in the forward and reverse direction from 1 μ A to 100 mA across ports 1 and 4, as shown in Fig. 1. The voltage was acquired by a Keithley 2182 nanovoltmeter. One channel measured and the other channel (not shown) measured the voltage drop across the 1.2 Ω resistor in series with the sample. The voltage across the resistor was used to precisely determine the bias current flowing through the device.

B. Sample Characterization

Bare samples of dimension 2 mm \times 10 mm \times 0.4 mm were prepared by dicing a 2-inch diameter n -type GaAs wafer with the [001] growth direction along the 10 mm side. Gallium arsenide was chosen because it is a direct gap^{10,11} (1.424 eV at 300 K) semiconductor and because of optimal absorption in the spectral region of the argon ion laser. The sample was degenerately doped¹² with Si at a concentration $N_D = 1.25 \times 10^{18}$ cm⁻³. The elec-

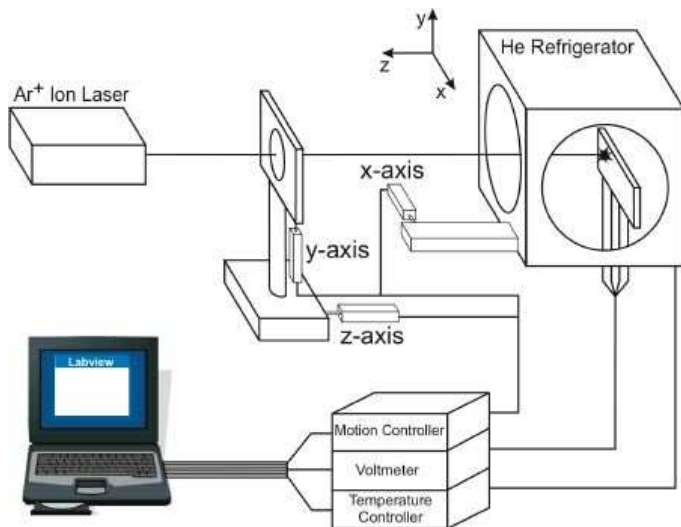


FIG. 2: (Color online) A schematic diagram of the experimental setup for sample positioning and data acquisition.

tron mobility of the semiconductor was measured to be $2100 \text{ cm}^2/\text{Vs}$. Leads were attached first by metalizing the GaAs, in an inert nitrogen atmosphere, with dots of In (of diameter $\sim 0.2 \text{ mm}$) arranged along the 10 mm side (see Fig. 2). Indium was chosen for metalizing because of its low melting temperature and compatibility with GaAs.¹³ This setup is similar to the typical four-lead van der Pauw plate setup used elsewhere.¹⁴ Next, the wires were tinned with In and pressed onto the metalized In dots. Ohmic contacts over the temperature range of interest were confirmed by verifying the linearity of the measured I-V response. These same bare samples were then used to make hybrid samples via the addition of an In shunt. This was achieved by metalizing the bare samples on the side opposite the leads with Indium of dimensions $10 \text{ mm} \times 0.5 \text{ mm} \times 0.5 \text{ mm}$. The hybrid sample resistance at room temperature, as measured across ports 1 and 4, decreased by an order of magnitude from that of the bare samples, indicating the effectiveness of the shunt. Ohmic contact at the interface was again verified by the linearity of the I-V response.

C. Experimental Procedure

Once the sample position was calibrated, the positional dependence of the voltage V_{23} was studied by moving the laser spot along the x -direction for fixed values of y_ℓ . However, in no case was the interface between the semiconductor and the shunt illuminated by the focused laser beam. Voltages were read every 0.1 mm in the x -direction which provided adequate resolution. Upon reaching the end of the sample, the x -position was returned to zero and the y -position was incremented by 0.1 mm . The program Labview was used to control the sample position and to acquire the data. The experi-

ments were performed under the same conditions for the bare sample and the MSH in order to produce consistent results. The position-dependent data acquisition, as outlined above, was repeated for various temperatures, bias currents, and power densities.

III. THEORETICAL MODEL

When the laser illuminates a circular region of radius r_s , at a position (x_ℓ, y_ℓ) , electron-hole pairs are created within the region and the individual carriers diffuse away from the spot center. As noted by Dember¹⁵ many years ago, the electrons, which have a much higher mobility than the holes ($\mu_e/\mu_h \sim 20$ in GaAs),¹⁶ diffuse away more rapidly from the focal spot region which causes an excess steady state positive charge to develop there. Outside the focal region, the diffusing carriers eventually recombine due to a number of processes. Nevertheless, the excess charge in the focal region perturbs the potential at the voltage probes and this perturbation depends, not only on the position of the focal spot but also on a number of other factors, such as temperature, excitation wavelength, power density, etc. Most importantly, the voltage probe perturbation also depends on the proximity to the shunt that, if present, enhances the removal of the photo-induced carriers and thus quantitatively affects the magnitude of the excess charge in the focal region. The processes described above can be modeled using the semiconductor drift-diffusion equations with terms that account for photo-generation and recombination. The electric field appearing in these equations is obtained from the solution of the Poissons equation with the excess carriers as the source terms.

A. The Drift-Diffusion Equations

Following the arguments of McKelvey¹⁷ and Chuang,¹⁸ when photo-generated carriers are present, the current has the usual resistive and diffusive terms,

$$\vec{J}_n = q(\mu_n n \vec{E} + D_n \vec{\nabla} n) \quad (2)$$

$$\vec{J}_p = q(\mu_p p \vec{E} - D_p \vec{\nabla} p), \quad (3)$$

where n and p represent the electron and hole number densities and μ_n and μ_p are their respective mobilities. The quantity $q = |e|$ is the magnitude of the electron charge. The quantities D_n and D_p are the diffusion coefficients defined by the Einstein relations,

$$D_n = \frac{\mu_n k_b T}{q} \quad (4)$$

$$D_p = \frac{\mu_p k_b T}{q}. \quad (5)$$

The effects of recombination and e-h pair generation must be taken into account in the equations of continuity so

that we have

$$\frac{1}{q} \vec{\nabla} \cdot \vec{J}_n + G(x, y) - R_n(x, y) = \frac{\partial n}{\partial t} \quad (6)$$

$$-\frac{1}{q} \vec{\nabla} \cdot \vec{J}_p + G(x, y) - R_p(x, y) = \frac{\partial p}{\partial t}, \quad (7)$$

where $G(x, y)$ is the spatially dependent generation rate per unit volume, and $R_n(x, y)$, $R_p(x, y)$ are the recombination rates for electrons and holes.

Using Eqs. (2) and (3) in the above equations gives the steady state semiconductor drift-diffusion equations,

$$\vec{\nabla} \cdot (D_n \vec{\nabla} n + \mu_n n \vec{E}) + G(x, y) - R_n(x, y) = 0 \quad (8)$$

$$\vec{\nabla} \cdot (D_p \vec{\nabla} p - \mu_p p \vec{E}) + G(x, y) - R_p(x, y) = 0 \quad (9)$$

The carrier number densities can be written as $n = n_o + \bar{n}$ and $p = p_o + \bar{p}$. In the case at hand, the materials are n -type with $p_o \cong 0$, and the equilibrium electron number density n_o is much larger than the excess electron density \bar{n} . As noted above, in GaAs the electron mobility is roughly 20 times larger than that of holes. As a result, the excess electrons diffuse away rapidly from the laser spot and therefore can be viewed as a small increase in the large equilibrium electron density. Moreover, since $p_o \cong 0$, the hole number density is simply equal to the excess hole number density \bar{p} , in which case the drift-diffusion equation for holes is,

$$\vec{\nabla} \cdot (D_p \vec{\nabla} \bar{p} - \mu_p \bar{p} \vec{E}) + G(x, y) - R_p(x, y) = 0, \quad (10)$$

where the quantity \vec{E} is the local electric field. The recombination rate for holes is assumed to be proportional to the hole number density, $R_p = \frac{\bar{p}(x, y)}{\tau}$, where $\tau = 0.5$ ns is the carrier recombination time¹⁸ used in our calculations. The generation rate $G(x, y)$ is assumed to be a Gaussian, with the average radius being equal to the spot radius of the illuminating laser

$$G(x, y) = G_o \exp \left[-\frac{\pi}{4} \left(\frac{r}{r_s} \right)^2 \right]. \quad (11)$$

Here G_o is the generation rate per unit volume at the spot center, and the value of the coordinate r is relative to the spot center position (x_ℓ, y_ℓ) . The drift diffusion equation for holes is now given by

$$\vec{\nabla} \cdot (D_p \vec{\nabla} \bar{p} - \mu_p \bar{p} \vec{E}) + G_o \exp \left[-\frac{\pi}{4} \left(\frac{r}{r_s} \right)^2 \right] - \frac{\bar{p}}{\tau} = 0, \quad (12)$$

In order to solve Eq. (12), we set (a) $\bar{p} = 0$ on the current ports 1 and 4, and (b) $\bar{p} = 0$ in the metallic shunt region. The first boundary condition asserts that any net hole distribution on the current ports will recombine with the electrons in the Indium leads. The second boundary condition is due to the fact that the shunt is metallic and therefore any hole states will be short lived. These boundary conditions are straightforward to implement within the framework of the FEM. Figure 3 shows the hole distribution for both the bare and shunted device. The hole distribution for the bare device is delocalized as compared to that of the shunted device.

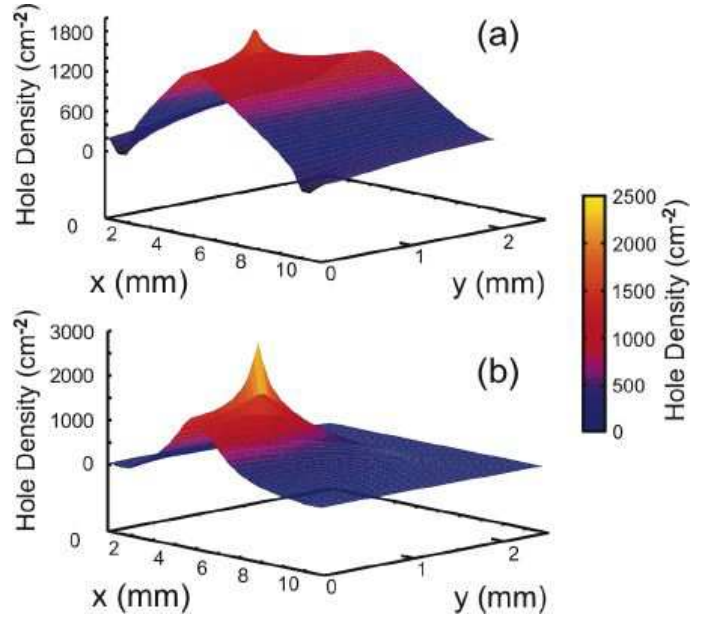


FIG. 3: (Color online) Excess hole density in (a) the bare device and (b) the MSH device at the laser spot position $(x_\ell, y_\ell) = (4\text{mm}, 0.7\text{mm})$.

B. The Finite Element Method

The solution of Eq. (12) is obtained using the Galerkin FEM,^{19,20} with the weight functions being the same functions as the interpolation polynomials used to represent the number density \bar{p} in each finite element. Multiplying Eq. (12) by the Galerkin weight function $\phi(x, y)$ and integrating gives

$$\iint \phi \vec{\nabla} \cdot (D_p \vec{\nabla} \bar{p} - \mu_p \bar{p} \vec{E}) dA - \iint \phi \frac{\bar{p}}{\tau} dA = -G_o \iint \phi \exp \left[-\frac{\pi}{4} \left(\frac{r}{r_s} \right)^2 \right] dA. \quad (13)$$

The first integral in the above equation is integrated by parts to yield

$$\begin{aligned} & - \iint \vec{\nabla} \phi \cdot (D_p \vec{\nabla} \bar{p} - \mu_p \bar{p} \vec{E}) dA + \\ & \oint \phi (D_p \vec{\nabla} \bar{p} - \mu_p \bar{p} \vec{E}) \cdot \hat{n} dl - \iint \phi \frac{\bar{p}}{\tau} dA = \\ & -G_o \iint \phi \exp \left[-\frac{\pi}{4} \left(\frac{r}{r_s} \right)^2 \right] dA. \end{aligned}$$

The second term, the surface term, in the above equation represents a flux of holes through the external boundary and is included only at the current ports in Fig. 1(c). The hole current at the current ports can be calculated using

$$I_{port} = qd \int_{port} D_p \vec{\nabla} \bar{p} \cdot \hat{n} dl, \quad (14)$$

where d is the thickness of the sample. These diffusive currents must be included in determining the net current flowing through the device. The applied voltage necessary for maintaining the net current at its given value is calculated by determining the effective device resistance including all carriers. This voltage is applied as the boundary condition for the Poisson equation,

$$\vec{\nabla} \cdot (\varepsilon \vec{\nabla} V) = -q\bar{p}, \quad (15)$$

where ε is the material permittivity. Equation (15) is solved using the Galerkin FEM for the electrostatic potential due to the excess hole density with the boundary conditions that the applied voltage mentioned above is applied across the current ports 1 and 4, while the voltages at ports 2 and 3 (see Fig. 1) are determined by the solution.

The steps for calculating the potential due to the photo-generated carriers are outlined below for one laser spot position:

1. Solve the drift-diffusion equation for $\bar{p} = 0$ (Eq. 12).
2. Calculate the current on the input and output current ports (Eq. 14).
3. Determine the applied voltage V_{14} from the requirement that the net current be the given current through the device.
4. Solve Eq. (15) with V_{14} applied across the current ports.
5. Calculate the voltage difference V_{23} between the voltage ports using the solution of Eq. (15) from the last step.

IV. RESULTS AND DISCUSSION

A. Dependence of EOC on Laser Spot Position

The measured voltage V_{23} and theoretical results (solid lines) are shown in Fig. 4 for $y_\ell = (0.2 \text{ mm and } 0.7 \text{ mm})$ as a function of x_ℓ for both the hybrid and bare samples at a temperature of 15 K with a power density of $6.3 \times 10^4 \text{ W/cm}^2$. The theoretical shape of the hole distribution is governed by the mobility, and thus the mean free path. The mean free path is calculated from

$$l = v_F \tau = \left(\frac{\hbar}{m^*} \right) k_F \left(\frac{\mu m^*}{e} \right) = \hbar \sqrt{2\pi n t} \left(\frac{\mu}{e} \right), \quad (16)$$

which takes into account the Fermi velocity, v_F , Fermi wave vector, k_F , scattering time, τ , effective mass, m^* , mobility, μ , thickness, t , of the sample, and the volumetric carrier density, n . As x_ℓ increases there is a peak (valley) corresponding to the positive V_2 (negative

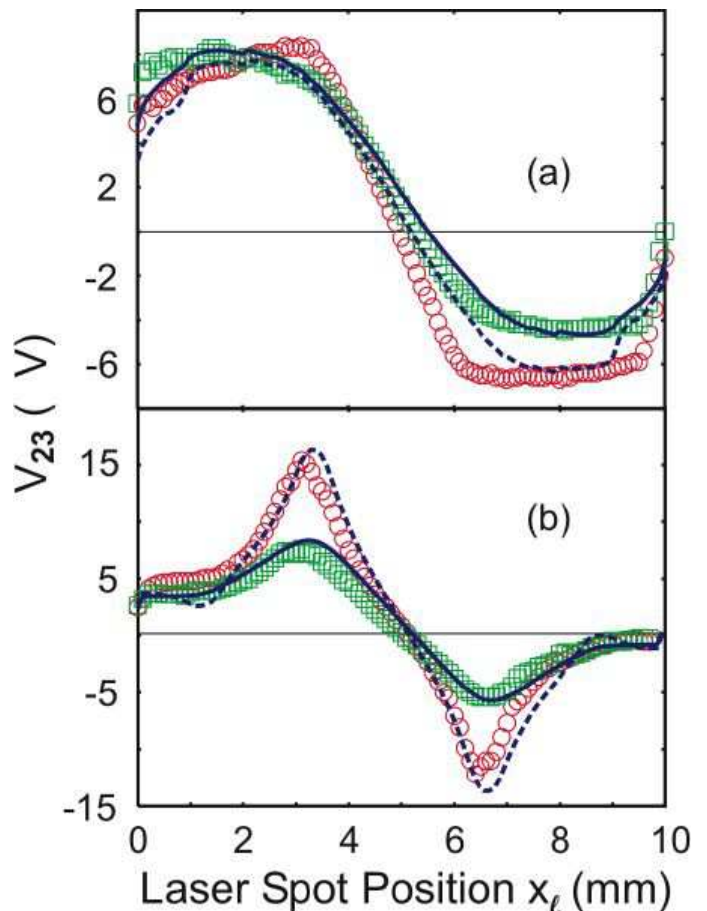


FIG. 4: (Color online) Voltage as the laser spot is moved in the x -direction for $y_\ell = 0.2 \text{ mm}$ (\circ , $- - -$) and $y_\ell = 0.7 \text{ mm}$ (\square , $-$) the bare sample (a) and the MSHs (b). The curves represent theoretical calculations and the points represent experimental measurements. Experimental measurements were taken at 15 K with a power density of $6.3 \times 10^4 \text{ W/cm}^2$.

V_3) voltage lead. As is evident in Fig. 4, the theoretical model reasonably approximates the positional dependence along the x -direction. The generation rate G_o , which was the only adjustable parameter, was varied such that the measured and calculated voltages coincided at the peak value. The value of the voltage at other x_ℓ positions was determined using the same generation rate which was used to match the peak value. This process of choosing the generation rate was done separately for each value of y_ℓ and for both the bare and shunted sample.

Figure 5 shows the voltage V_{23} for $x_\ell = 3.3 \text{ mm}$ as a function of y_ℓ , for both the hybrid and bare sample with theory represented by solid and dashed lines. As y_ℓ increases, the absolute value of the voltage approaches zero for both the hybrid and bare samples. In addition, with increasing y_ℓ , the charge distributions are further away from the voltage leads and closer to the shunt, thereby lowering the measured voltage. As a result, the voltage in the hybrid sample decreases as the laser spot is moved closer to the shunt. Because of these effects, both V_{23} and

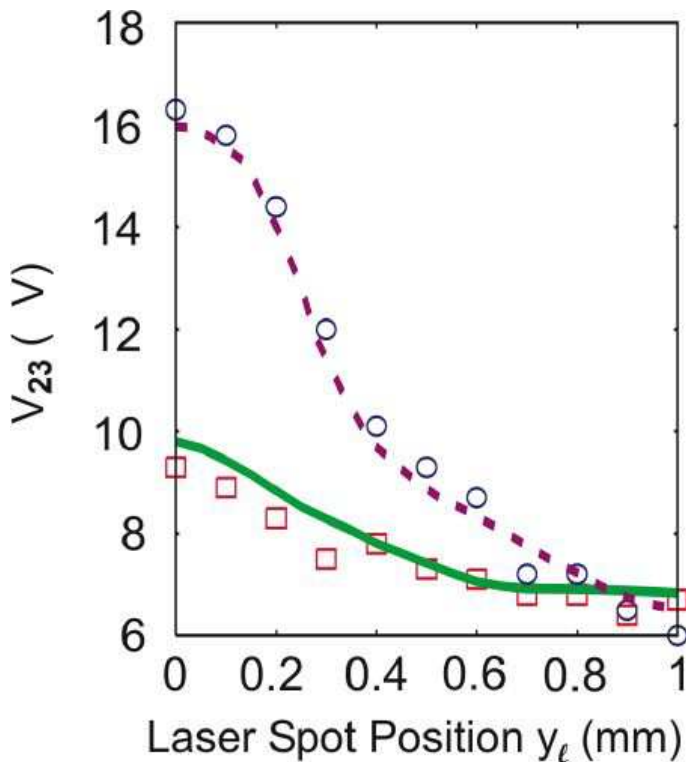


FIG. 5: (Color online) Voltage as the laser spot is moved in the y -direction for $y_\ell = 3.3$ mm for the bare sample (\square ,—) and MSHs (\circ , - - -). The curves represent theoretical calculations and the points represent experimental measurements. Relevant experimental parameters are given in Fig. 4 caption.

the EOC decrease as a function of the y position, with its peak being at $y_\ell = 0$. Similar to the x_ℓ dependence, one generation rate for the y_ℓ dependence was chosen such that the theoretical voltages matched the experimental values over the entire range of y_ℓ values.

B. EOC Dependence on the Bias Current

The voltages in both the hybrid and bare samples show an offset such that when the laser is not illuminating the sample, the measured voltage is nonzero. The voltage offset was seen to be additive to the voltage produced by the excess carriers over the range of bias current studied. In order to calculate the EOC, the offset was removed for both the bare sample and the MSH so that the data reflects the effect of the excess carriers alone. In addition, the voltage offset was found to be proportional to the bias current which suggests that it is associated with the intrinsic sample resistance and not the perturbation that we are interested in.

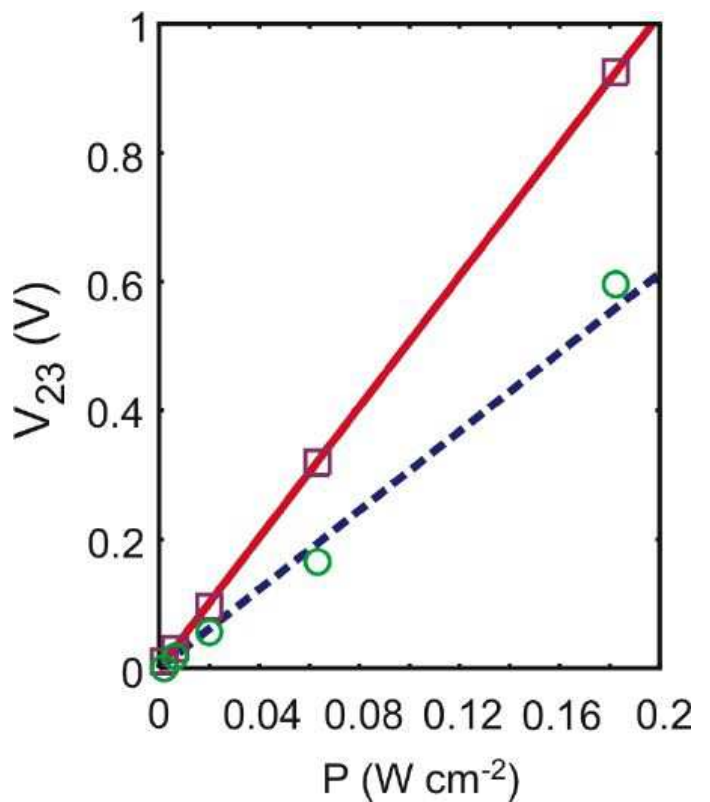


FIG. 6: (Color online) Voltage versus laser power at spot position $(y_\ell, x_\ell) = (3.3\text{mm}, 0\text{mm})$ for the bare sample (\square ,—) and MSHs (\circ , - - -). The lines represent theoretical calculations and the points represent experimental measurements. The voltage has a linear dependence on the laser power and the generation rate. The coefficient of proportionality is $\alpha_{bare} = 4 \times 10^{18} \text{ J}^{-1}\text{cm}^{-1}$ for the bare device and $\alpha_{shunt} = 1 \times 10^{19} \text{ J}^{-1}\text{cm}^{-1}$ for the shunted device. Experimental measurements were taken at 300 K.

C. EOC and Laser Power Dependence

The graph in Fig. 6 shows a plot of the dependence of V_{23} on the illuminating optical power density P . The theoretical curves indicate that the measured voltage depends linearly on the generation rate. Similarly, the experimental data indicates that the measured voltage depends linearly on the optical power density. These two observations suggest that the generation rate is proportional to the incident power, as should be expected in this regime. For the bare device, the coefficient of proportionality is $\alpha_{bare} = 4 \times 10^{18} \text{ J}^{-1}\text{cm}^{-1}$, and for the shunted device the coefficient is $\alpha_{shunt} = 1 \times 10^{19} \text{ J}^{-1}\text{cm}^{-1}$. The difference in α for the two devices arises from geometric contributions which affect the generation and recombination of carriers. Note that the range of power spans approximately two orders of magnitude.

D. EOC and Temperature Dependence

As reported⁹ previously, the EOC reaches a maximum of almost 500% at 30 K for optimal (x_ℓ, y_ℓ) values. The EOC also displays an inverse relationship with temperature. Here we will quantify and further elucidate that relationship.

Because the GaAs is degenerately doped, the equilibrium carrier concentrations (n_o, p_o) change minimally over the temperature range studied.²² The electron mobility²² and dielectric constant¹⁶ are also assumed constant over that temperature range. Implicit in the diffusion and resistive terms in Eq. 3 is a temperature dependence. According to Lovejoy *et al.*²² the hole mobility, μ_p , has an inverse temperature dependence that can be fit as $\mu_p = \chi T^{-\frac{3}{2}}$ where χ is a fixed parameter used to fit the data. In Eq. 5, we see an explicit linear temperature dependence of the diffusion coefficient. Thus the combined temperature dependence from Eq. 5 yields $D_p \sim T^{-\frac{1}{2}}$. As a result, the effect of the diffusive component decreases with increasing temperature.

Figure 7 shows the temperature dependence of the EOC for various y_ℓ values with a power density of $6.3 \times 10^4 \text{ W/cm}^2$ at $\lambda = 476.5 \text{ nm}$ and $x_\ell = 3.3 \text{ mm}$ with the points obtained from experiment and the curves calculated from the model. In the model, the generation rate was held constant for the bare GaAs sample, while G_o for the MSH was scaled to fit the EOC value at one temperature. With G_o fixed for each y_ℓ in this manner, the temperature dependence of the EOC was then calculated by simply incrementing the temperature. This temperature change, as discussed above, was incorporated directly into the diffusion coefficients as well as the hole mobility. With the exception of $y_\ell = 0 \text{ mm}$ and 0.2 mm , the EOC was fitted at 15K. These two y_ℓ values were fitted at 30 K as their 15 K data (shown) was deemed errant owing to the difficulty of establishing the $y_\ell = 0$ position, as discussed previously.⁹

E. EOC and the lateral photovoltaic effect

Because of the similarity in experimental setup and positional response to laser illumination between EOC and the well known lateral photovoltaic effect (LPE),²³ a discussion highlighting the differences is appropriate. Critical to the discussion of EOC and LPE is the illumination of the junction. The lateral photovoltaic effect requires illumination of the junction between a (doped) semiconductor and a metal or a heavily doped (conducting) semiconductor, using a configuration in which the illuminating beam is incident normal to the plane of the junction.²⁴ In contrast, in the EOC effect, the junction is NOT illuminated by the incident laser beam, which is incident parallel to the plane of the junction. Also, the LPE relies on a Schottky barrier at the metal-semiconductor interface, while for the EOC devices shown here, the interface is an ohmic contact.

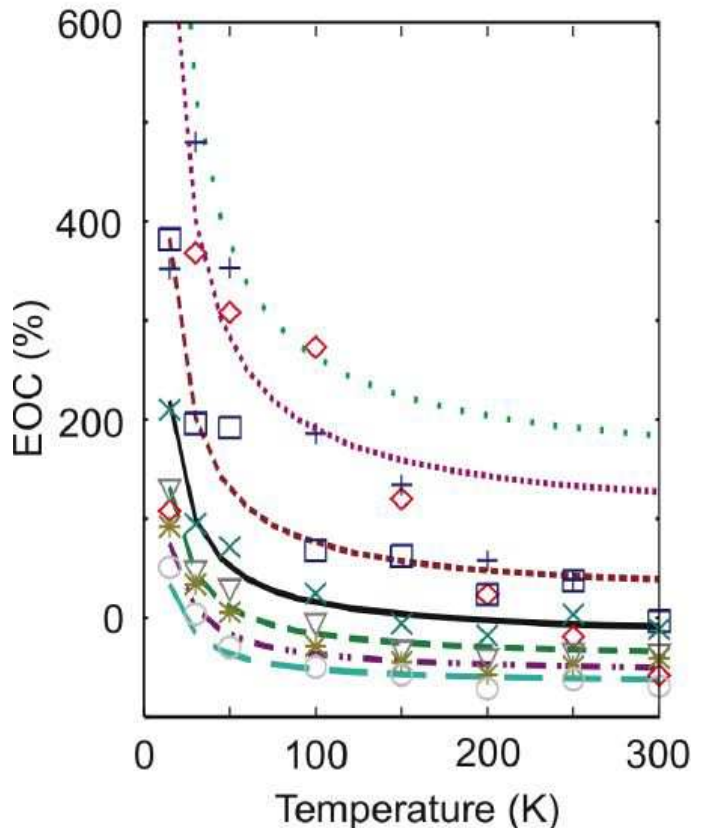


FIG. 7: (Color online) The temperature dependence of the EOC as defined by Eq. (1). The measurements were acquired at spot positions $x_\ell = 3.3 \text{ mm}$ with $y_\ell = 0 \text{ mm}$, (\diamond , $\cdot \cdot \cdot$); $y_\ell = 0.2 \text{ mm}$, ($+$, $\cdot \cdot \cdot$); $y_\ell = 0.4 \text{ mm}$, (\square , $- - -$); $y_\ell = 0.6 \text{ mm}$, (\times , solid); $y_\ell = 0.8 \text{ mm}$, (∇ , $- - -$); $y_\ell = 1.0 \text{ mm}$, ($*$, $- \cdot \cdot -$); and $y_\ell = 1.2 \text{ mm}$, (\circ , $- - -$) Experimental measurements were taken with a power density of $6.3 \times 10^4 \text{ W/cm}^2$.

Beginning with Wallmark²³ all theoretical analyses of the LPE are based on carrier dynamics derived from the photocurrent generated across the junction whereas our analysis, as explained above, is based primarily on the Dember effect and provides a very good fit to the position dependent voltage (see Figs. 4 & 5). Thus, despite the similarity of the positional dependence of the voltage response seen in some LPE measurements and ours, it should be clear that the EOC is a different phenomenon.

In the LPE, the output voltage at any lateral position of the illumination INCREASES with decreasing temperature.^{24,25} In the EOC effect in GaAs-In, the output voltage DECREASES with decreasing temperature. Our theoretical model provides a good fit to the temperature dependence of the EOC (see Fig. 7). This further supports the fact that EOC and LPE are fundamentally different position dependent effects.

V. CONCLUSION

The drift diffusion model of EOC has been successfully employed to fit experimental data taken using GaAs-In MSH structures. The model based on the FEM closely fits the voltage data and the resulting EOC calculation. The position dependence in x and y is incorporated in the model via the drift diffusion equation for holes based on the mean free path, and thus the mobility. By including a generation and recombination rate a reasonable fit was obtained. The model also reproduced the decrease in EOC with increasing $y\ell$. The EOC decreases with increasing temperature T , which the model directly accounts for through the temperature dependence of the mobility and the diffusion coefficients.

As mentioned briefly in our preliminary report⁹ EOC is similar to but fundamentally different from the well known lateral photovoltaic effect (LPE). The main difference lies in the fact that the interface is not illuminated in EOC, whereas in the LPE such illumination is critical. Moreover, because of the many factors influencing the EOC, it presents a unique opportunity to study and model the dynamics of the metal-semiconductor interface, carrier transport phenomena, and the effect of introducing a shunt.

Because the carrier mobilities are critical in the Dember effect, InSb should yield a two orders of magnitude increase in the observed EOC, possibly even room temperature EOC, as compared to GaAs. Using the drift diffusion model, we anticipate modeling the EOC of this direct gap semiconductor and others. We have not experimentally or theoretically optimized for wavelength, geometry of the device, or material parameters. With the new ability to model EOC as shown, predictions can be made to maximize the gain of an EOC device. Once optimized, we may expect MSH devices based on EOC to impact optical sensing technology, particularly position sensitive detectors.

Acknowledgments

The authors would like to thank Professor S. E. Hayes and Professor D. L. Rode for providing and dicing the GaAs samples. We also thank Yue Shao for useful discussions. This work is supported by the US National Science Foundation under grant ECS-0329347. LRR acknowledges support from Washington University in St. Louis which supported his collaborative visit during part of which this work was carried out.

-
- * Electronic address: solin@wustl.edu
- ¹ A. C. H. Rowe and S. A. Solin, Phys. Rev. B **71**, 235323 (2005).
 - ² S. A. Solin, D. R. Hines, A. C. H. Rowe, J. S. Tsai, Yu. A. Pashkin, S. J. Chung, N. Goel and M. B. Santos, Appl. Phys. Lett. **80**, 4012 (2002).
 - ³ S. A. Solin, D. R. Hines, T. Thio and J. Heremans, Science **289**, 1530 (2000).
 - ⁴ T. Zhou, D. R. Hines, and S. A. Solin, Appl. Phys. Lett. **78**, 667 (2001).
 - ⁵ J. Moussa, L. R. Ram-Mohan, J. Sullivan, T. Zhou, D. R. Hines, and S. A. Solin, Phys. Rev. B **64**, 184410 (2001).
 - ⁶ J. Moussa, L. R. Ram-Mohan, A. C. H. Rowe, and S. A. Solin, J. Appl. Phys. **94**, 1110 (2003).
 - ⁷ S. A. Solin, D. R. Hines, J. S. Tsai, Y. A. Pashkin, S. J. Chung, N. Goel, and M. B. Santos, IEEE Trans. Magn. **38**, 89 (2002).
 - ⁸ A. C. H. Rowe, D. R. Hines and S. A. Solin, Appl. Phys. Lett. **83**, 1160 (2003).
 - ⁹ K. Wieland, Yun Wang, L. R. Ram-Mohan, S. A. Solin, and A. M. Girgis, Appl. Phys. Lett., **88** 52105 (2006).
 - ¹⁰ S. M. Sze, *Physics of Semiconductor Devices*, 2nd ed. (Wiley, New York, 1981).
 - ¹¹ I. Vurgaftman, J. R. Meyer, and L. R. Ram-Mohan, J. Appl. Phys. **89**, 5815 (2001).
 - ¹² K. Seeger, *Semiconductor Physics*, (Springer-Verlag, Berlin, 1985, 3rd edition).
 - ¹³ A. A. Lakhani, J. Appl. Phys. **56**, 1888 (1984).
 - ¹⁴ L. J. van der Pauw, "A Method of Measuring Specific Resistivity and Hall Effect of Discs of Arbitrary Shapes," Philips Res. Repts. **13**, 1-9 (1958); L. J. van der Pauw, "A Method of Measuring the Resistivity and Hall Coefficient on Lamellae of Arbitrary Shape," *ibid.* **20**, 220-224 (1958).
 - ¹⁵ H. Dember, Phys. Z. **32**, 554 (1931).
 - ¹⁶ O. Madelung, editor, *Data in Science and Technology: Semiconductors Group IV Elements and III-V Compounds* (Springer-Verlag, New York, 1991).
 - ¹⁷ J. P. McKelvey, *Solid State and Semiconductor Physics* (Harper and Row, NY, 1966), Ch. 10.
 - ¹⁸ S. L. Chuang, *Physics of Optoelectronic Devices* (Wiley-Interscience, NY, 1995).
 - ¹⁹ L. R. Ram-Mohan, *Finite Element and Boundary Element Applications in Quantum Mechanics*, (Oxford University Press, Oxford, UK, 2002).
 - ²⁰ O. C. Zienkiewicz, *The Finite Element Method* (McGraw-Hill, New York, 1989); O. C. Zienkiewicz and R. L. Taylor, *The Finite Element Method* (McGraw-Hill, New York, 1994).
 - ²¹ W. Zawadzki, Adv. Phys. **23**, 435 (1974).
 - ²² M. L. Lovejoy, M. R. Melloch, and M. S. Lundstorm, Appl. Phys. Lett. **67**, 1101 (1995).
 - ²³ J. T. Wallmark, Proc. IRE **45** 474 (1957).
 - ²⁴ G. Lucovsky, J. Appl. Phys. **31**, 1088 (1960).
 - ²⁵ D. A. Redfern, W. Fang, K. Ito, G. Bahir, C. A. Musca, J. M. Dell and L. Faraone, J. Appl. Phys. **98**, 34501 (2005).